coatings

MDPI

Article

Oxidation Behavior of Ta–Al Multilayer Coatings

Yung-I Chen [1,2,3,*], Nai-Yuan Lin [1] and Yi-En Ke [2]

1 Institute of Materials Engineering, National Taiwan Ocean University, Keelung 20224, Taiwan; magickingzx@yahoo.com.tw
2 Department of Optoelectronics and Materials Technology, National Taiwan Ocean University, Keelung 20224, Taiwan; idstolen12@gmail.com
3 Center of Excellence for Ocean Engineering, National Taiwan Ocean University, Keelung 20224, Taiwan
* Correspondence: yichen@mail.ntou.edu.tw; Tel.: +886-2-2462-2192

Received: 31 October 2019; Accepted: 29 November 2019; Published: 1 December 2019

Abstract: Ta–Al multilayer coatings were fabricated through cyclical gradient concentration deposition by direct current magnetron co-sputtering. The as-deposited coatings presented a multilayer structure in the growth direction. The oxidation behavior of the Ta–Al multilayer coatings was explored. The results specified that Ta-rich Ta–Al multilayer coatings demonstrated a restricted oxidation depth after annealing at 600 °C in 1% O_2–99% Ar for up to 100 h. This was attributed to the preferential oxidation of Al, the formation of amorphous Al-oxide sublayers, and the maintenance of a multilayer structure. By contrast, Ta_2O_5 formed after exhausting Al in the oxidation process in an ambient atmosphere at 600 °C which exhibited a crystalline Ta_2O_5-amorphous Al-oxide multilayer structure.

Keywords: cyclical gradient concentration; internal oxidation; multilayer coating; oxidation

1. Introduction

Al-based inter-metallics have been used for high-temperature applications because of their high melting points, strength, and oxidation resistance [1–14]. For example, Ru–Al alloys have been applied for jet engine components, bond coats for thermal barrier coatings, corrosion- and oxidation-protective coatings, and electrodes [1,2], whereas Ta–Al alloys have been applied for sulfidation and oxidation-protective coatings [3–5], heater materials [12–14], and electromagnetic shielding [15]. A previous paper [16] evaluated the oxidation behavior of Ru–Al multilayer coatings in 1% O_2–99% Ar at 400–800 °C. In our co-sputtering system [16–21], the plasma sources focused on a circular track but not the center of the substrate-holder; thus, a multilayer coating with cyclical gradient concentration formed, as the substrate-holder was rotated in a low speed of 1–7 rpm. Such multilayer coatings were constructed by alloy sublayers with continuous variation in compositions, but not monolithic sublayers of distinct elements. Additionally, the inward diffusion of oxygen during annealing resulted in the coating forming an internally oxidized multilayer structure comprising alternating oxygen-rich and oxygen-deficient sublayers. The execution of internal or external oxidation was affected by the annealing atmosphere and the diffusion of the active elements [17,22,23]. The internal and external oxidation of the Ru–Al multilayer coatings exhibited restricted oxidation depths and overcoats, respectively, which were attributed to the formation of continuous Al_2O_3 sublayers and scales [16]. The multilayer structure with O-saturated Al_2O_3 oxide sublayers benefited to inhibit further oxidation. Moreover, the Ru–Al multilayer films subjected to an ambient atmosphere at 800 °C exhibited a limited oxidation depth [24]. Considering the merits of oxidation resistance and cost reduction, the feasibility of Ta–Al to replace the Ru–Al multilayer coatings in high-temperature applications was evaluated. The oxidation behavior of the Ta–Al multilayer coatings with cyclical gradient concentrations prepared using direct current (DC) magnetron co-sputtering was investigated at 400–600 °C.

2. Materials and Methods

The Ta–Al coatings with a Ti interlayer were fabricated onto silicon wafers by DC magnetron co-sputtering. A previous study [18] illustrated the co-sputtering equipment and the experimental details such as the base pressure, working pressure, and Ar flow. The substrate holder was heated to 400 °C and rotated at 1 rpm. The Ti interlayer was deposited with a DC power of 200 W for 7 min. Then, Ta and Al were co-sputtered onto the Ti interlayer using various sputter powers for 35 min. The deposition rates of Ta and Al at a DC power of 200 W were 9.1 and 21.3 nm/min, respectively. The powers applied on Ta and Al targets were denoted as P_{Ta} and P_{Al}, respectively. The total powers of P_{Ta} and P_{Al} were fixed at 300 W. The annealing experiments were performed in 1% O_2–99% Ar at 400–600 °C for 0.5–100 h, or in air at 600 °C for 1–100 h.

A chemical composition analysis of the samples was conducted using a field-emission electron probe microanalyzer (FE-EPMA; JXA-8500F, JEOL, Akishima, Japan). The thickness evaluation of the coatings was performed using a field emission scanning electron microscope (FE-SEM; S4800, Hitachi, Tokyo, Japan). A conventional X-ray diffractometer (XRD; X'Pert PRO MPD, PANalytical, Almelo, The Netherlands) was adopted to identify the phases using the grazing incidence technique with an incidence angle of 1°. The nanostructure was examined using a transmission electron microscope (TEM; JEM-2010F, JEOL, Tokyo, Japan). The TEM samples with Pt protective layers were prepared by applying a focused ion beam system (FEI Nova 200, Hillsboro, OR, USA) which was transferred to Cu grids. An energy-dispersive spectrometry (EDS; Inca x-sight, Oxford Instruments, Tokyo, Japan) equipped with TEM was used to determine the local chemical compositions. The chemical composition depth profiles were evaluated using an Auger electron spectroscopy (AES; PHI700, ULVAC-PHI, Kanagawa, Japan). The sputter depths in the AES results were correlated with the thicknesses determined by the cross-sectional SEM images.

3. Results and Discussion

3.1. As-Deposited Ta–Al Coatings

Table 1 lists the sputtering parameters, chemical compositions, and thicknesses of the as-deposited Ta–Al coatings. These samples are denoted as $Ta_{0.33}Al_{0.67}$, $Ta_{0.61}Al_{0.39}$, and $Ta_{0.81}Al_{0.19}$ coatings. Figure 1 depicts these coatings exhibiting evident multilayer structures. The sputtering time was set at 35 min, and the total powers of P_{Ta} and P_{Al} were fixed at 300 W; therefore, the deposition rate increased with an increase in the power ratio of the Al target. Figure 2 exhibits the XRD patterns of the as-deposited and 1% O_2–99% Ar-annealed Ta–Al coatings. The as-deposited $Ta_{0.33}Al_{0.67}$ coatings exhibited a tetragonal $TaAl_3$ (ICDD 03–065–2665) phase and a cubic Al (ICDD 00–004–0787) phase, whereas the $Ta_{0.61}Al_{0.39}$ and $Ta_{0.81}Al_{0.19}$ coatings were composed of $TaAl_3$ and tetragonal β-Ta (ICDD 00–025–1280) phases. The β-Ta phase is metastable and is observed for the sputtered coatings [25–27]. The $TaAl_3$ has been reported to be the preferred aluminide phase in the Ta–Al system [14,28,29] with a formation enthalpy of −36 kJ/mol in the temperature interval of 1050–1350 K [29]. The Ta-rich and Al-rich Ta–Al films prepared at room temperature by Chung et al. [14] had $TaAl_3$–Ta and $TaAl_3$–Al phases, respectively, which exhibited polycrystalline structures. The Ta-rich films showed a remarkable thermal stability after having been annealed in a vacuum at 450–650 °C, whereas the Al-rich films exhibited a phase transformation at 450 °C [14]. Because the Ta–Al coatings in this study were prepared at 400 °C, no amorphous parts were observed in the as-deposited films.

Table 1. Sputtering parameters, chemical compositions, and thicknesses of the Ta–Al coatings.

Sample	Power		Chemical Composition (at.%)			Thickness (nm)
	P_{Ta} (W)	P_{Al} (W)	Ta	Al	O	
$Ta_{0.33}Al_{0.67}$	100	200	31.7 ± 0.4	64.5 ± 0.2	3.8 ± 0.2	1110
$Ta_{0.61}Al_{0.39}$	150	150	58.3 ± 0.4	37.3 ± 0.2	4.4 ± 0.4	884
$Ta_{0.81}Al_{0.19}$	200	100	76.8 ± 0.3	18.2 ± 0.1	5.0 ± 0.2	820

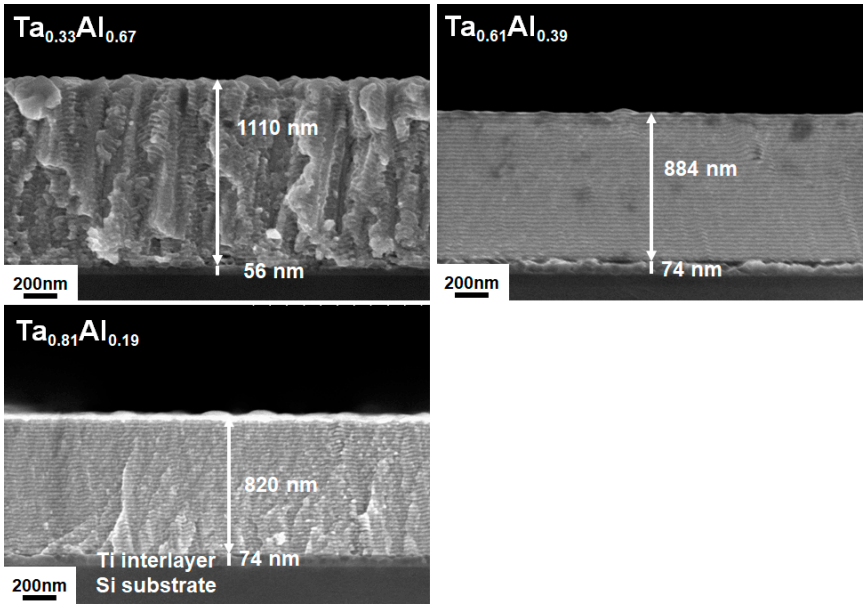

Figure 1. Cross-sectional SEM images of the as-deposited Ta–Al multilayer coatings.

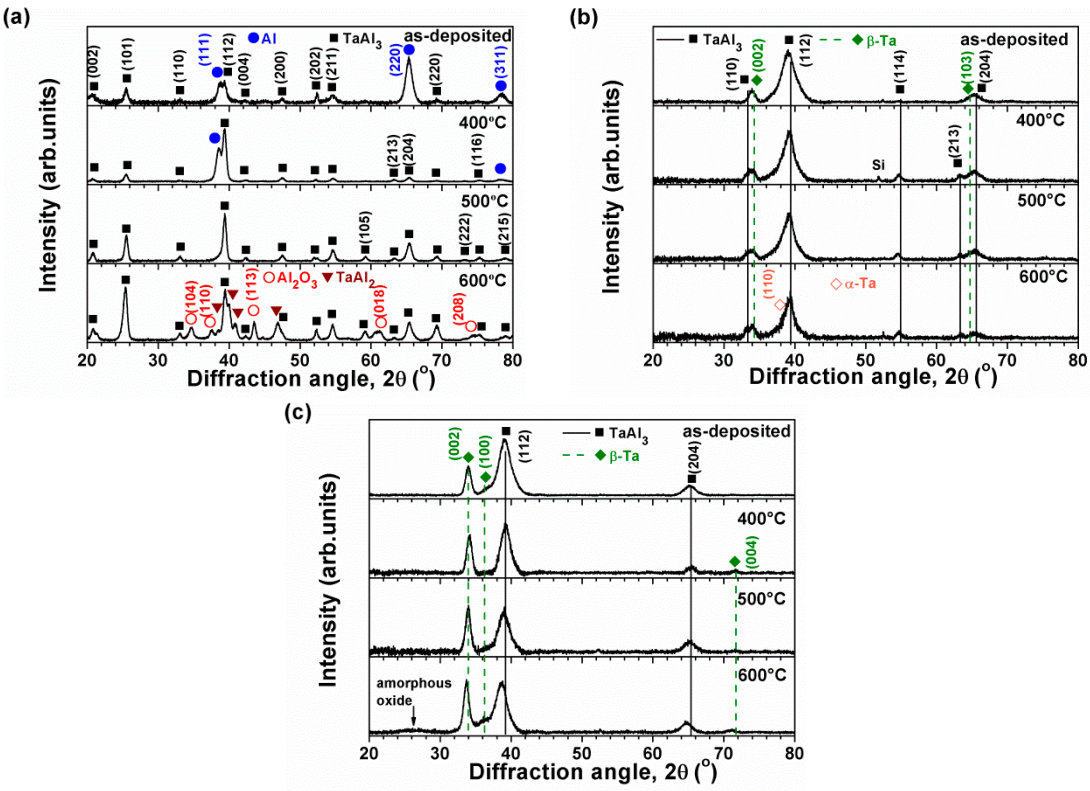

Figure 2. XRD patterns of the as-deposited and annealed (**a**) $Ta_{0.33}Al_{0.67}$, (**b**) $Ta_{0.61}Al_{0.39}$, and (**c**) $Ta_{0.81}Al_{0.19}$ coatings (annealing time: 30 min).

3.2. Oxidation of Ta–Al Coatings in 1% O_2–99% Ar

The as-deposited $Ta_{0.33}Al_{0.67}$ coatings comprised Al and $TaAl_3$ phases with a strong Al(220) reflection, whereas the coatings annealed at 400 °C exhibited a strong $TaAl_3$(112) reflection, and no Al phase was shown by the coatings annealed at 500 °C (Figure 2a). Moreover, the $Ta_{0.33}Al_{0.67}$ coatings annealed at 600 °C exhibited reflections of $TaAl_3$, $TaAl_2$ (ICDD 00–050–1279), and Al_2O_3 phases, accompanied with a granular structure, as shown in a cross-sectional SEM image (Figure 3). Because the standard Gibbs free energy levels for the formation of the metal oxides Al_2O_3 and Ta_2O_5 at 600 °C are −934,815 and −663,572 J/(mol of O_2) [30], respectively, Al_2O_3 is formed preferentially when the Ta–Al coatings are oxidized. The XRD patterns of the $Ta_{0.61}Al_{0.39}$ and $Ta_{0.81}Al_{0.19}$ coatings annealed in 1% O_2–99% Ar at 400–600 °C for 30 min exhibited reflections similar to those of the as-deposited coatings (Figure 2b,c). A cubic α-Ta (110) reflection (ICDD 00–004–0788) became clear for the $Ta_{0.61}Al_{0.39}$ coating that had been annealed at 600 °C, whereas one extra broadened reflection, which was attributed to surface oxidation, was observed for the $Ta_{0.81}Al_{0.19}$ coating that had been annealed at 600 °C. The annealed $Ta_{0.61}Al_{0.39}$ and $Ta_{0.81}Al_{0.19}$ coatings maintained multilayered structures (Figure 3); however, the two outermost stacking periods extended their widths. The thicknesses of the Ti interlayers increased after annealing which was attributed to the interdiffusion of the Ti interlayer and Si substrate [24].

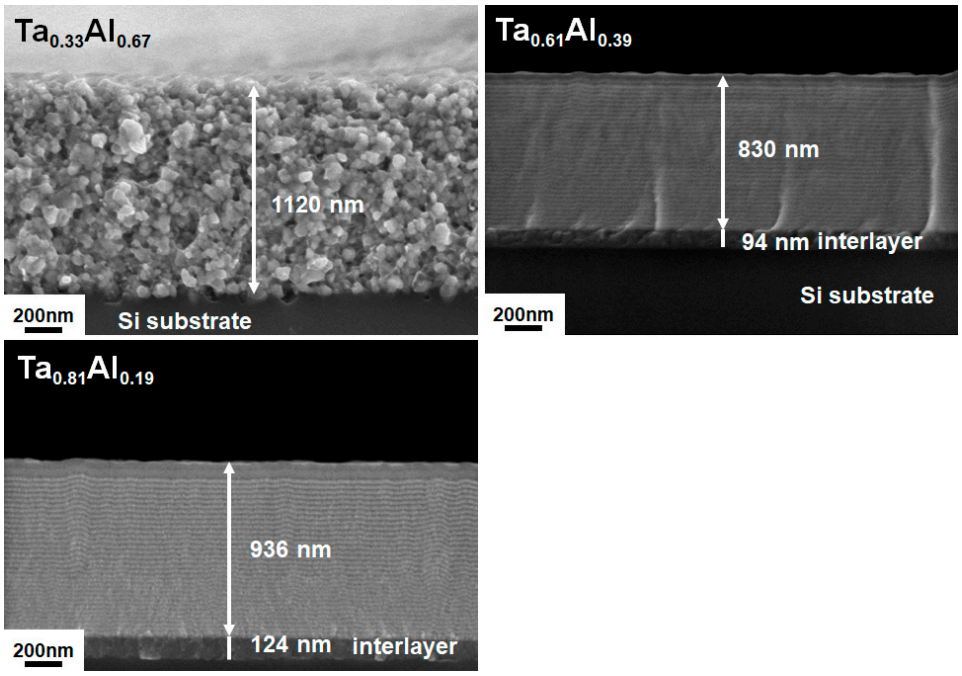

Figure 3. Cross-sectional SEM images of Ta–Al coatings annealed in 1% O_2–99% Ar at 600 °C for 30 min.

The cross-sectional TEM image (Figure 4a) of the $Ta_{0.61}Al_{0.39}$ coating annealed at 600 °C for 30 min exhibited a remaining multilayer structure. The EDS analysis verified that the inward diffusion of O tended to accumulate in the outmost stacking periods. The black sublayers (labelled as 1a, 2a, and 3a in Figure 4a) were dominated by Ta, whereas the white sublayers were enriched with Al and O. The selected area diffraction pattern (SADP) of the O-diffused region shows α-Ta and $TaAl_3$ rings without an evident oxide phase, suggesting that the Al oxide was amorphous. A high-resolution TEM image (Figure 4b) illustrates that the black sublayers were the α-Ta phase, whereas the crystalline $TaAl_3$ domains were identified between the Ta-rich sublayers and the amorphous Al-oxide sublayers. Figure 5 shows the AES results of the 600 °C and 4 h annealed $Ta_{0.61}Al_{0.39}$ coatings. The O diffusion depth was restricted to two or three of the stacking periods. The deviation of the AES analyzed atomic

concentration from that examined by EPMA could be attributed to the preferential sputtering effects which were also reported for the Ru–Al system [31,32]. Moreover, the fluctuation of the profiles in the deeper region seemed unclear, accompanied with a large sampling interval because of a sputter etching rate of 6.76 nm/min. Figure 6 exhibits the XRD patterns of the $Ta_{0.61}Al_{0.39}$ coatings annealed for 0.5–100 h. The XRD patterns of the $Ta_{0.61}Al_{0.39}$ coatings that were annealed for 30 min exhibited coexisting α-Ta and β-Ta phases, whereas the α-Ta phase was dominant for the films with annealing times exceeding 4 h; these results implied that the metastable β-Ta in the shallow depth region transformed to the stable α-Ta, because the XRD patterns were recorded using the grazing incidence technique. The XRD patterns of the 4, 12, and 24 h annealed $Ta_{0.61}Al_{0.39}$ coatings exhibited similar results. By contrast, amorphous oxide signals at two theta angles less than 30° can be observed for the $Ta_{0.61}Al_{0.39}$ coatings annealed for 50 and 100 h. Figure 7a shows the cross-sectional TEM image of a $Ta_{0.61}Al_{0.39}$ coating annealed for 100 h; the O signals detected by EDS were observed at the outmost nine stacking periods, accompanied with expanded period widths. The high-resolution TEM image (Figure 7b) illustrates that the black sublayers were an α-Ta phase, whereas the crystalline $TaAl_3$ domains were dispersed in the amorphous Al-oxide matrix, which formed the white sublayers. Because Al and Ta are insoluble in equilibrium states [33,34], and the Ta–Al coatings were fabricated through a cyclical gradient concentration deposition, the Ta-rich sublayers behaved as a diffusion barrier for Al at 600 °C. Thus, internal oxidation became the main oxidation mechanism, and the preferentially formed Al-oxide sublayers restricted oxidation. Therefore, the $Ta_{0.61}Al_{0.39}$ coatings that had been annealed up to 100 h exhibited thermal stability and oxidation resistance. By contrast, no Ta-rich sublayers formed during the sublayer stacking of the $Ta_{0.33}Al_{0.67}$ coatings. Thus, granular Al_2O_3 formed during annealing at 600 °C, and the multilayer structure was destroyed and partially detached.

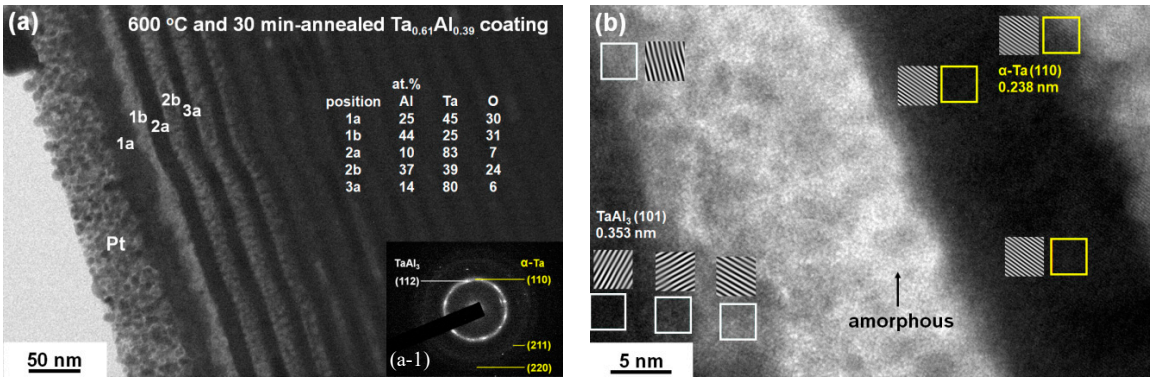

Figure 4. (**a**) Cross-sectional TEM image and (**a–1**) selected area diffraction pattern (SADP) and (**b**) high-resolution TEM image of the $Ta_{0.61}Al_{0.39}$ coating annealed in 1% O_2–99% Ar at 600 °C.

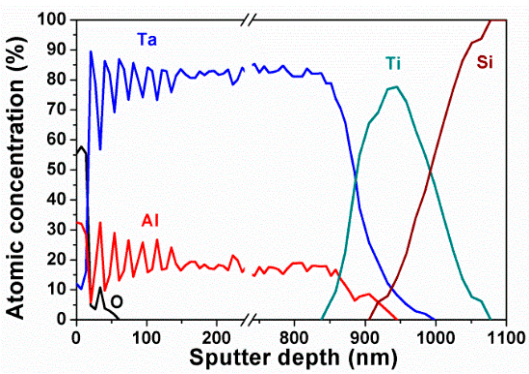

Figure 5. Auger electron spectroscopy (AES) depth profiles of $Ta_{0.61}Al_{0.39}$ coatings annealed in 1% O_2–99% Ar at 600 °C for 4 h.

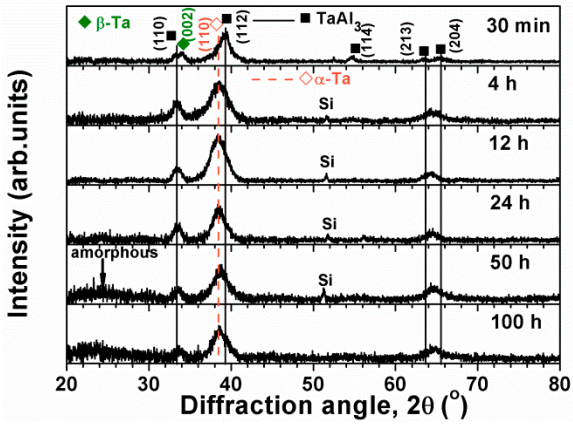

Figure 6. XRD patterns of $Ta_{0.61}Al_{0.39}$ coatings annealed in 1% O_2–99% Ar at 600 °C.

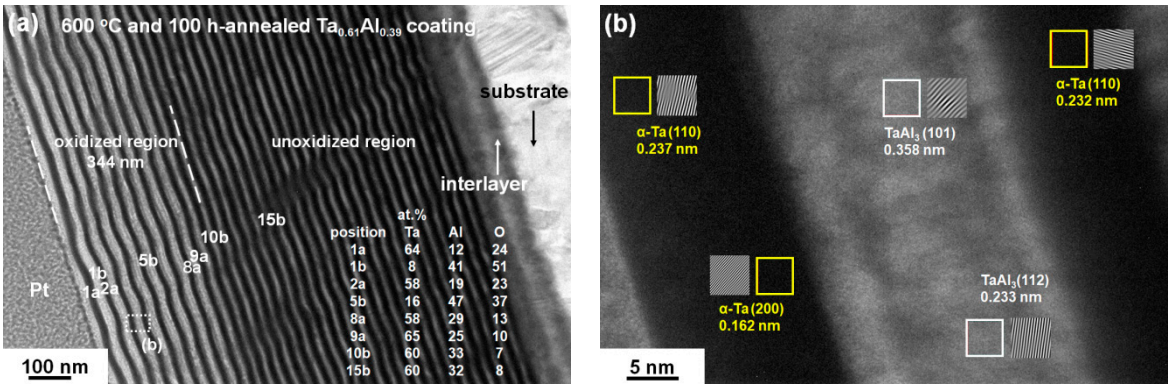

Figure 7. (**a**) Cross-sectional and (**b**) high-resolution TEM images of the $Ta_{0.61}Al_{0.39}$ coating annealed in 1% O_2–99% Ar at 600 °C for 100 h.

3.3. Oxidation of Ta–Al Coatings in Air

The $Ta_{0.63}Al_{0.37}$ coatings (60.8 at.% Al + 35.6 at.% Ta + 3.6 at.% O) were prepared using the same sputter parameters for fabricating $Ta_{0.61}Al_{0.39}$ coatings mentioned in Section 3.2. The two coatings belonged to two batches and exhibited a slight deviation in chemical compositions. Figure 8 shows the XRD patterns of the $Ta_{0.63}Al_{0.37}$ coatings annealed in air at 600 °C for 1–100 h. The $Ta_{0.63}Al_{0.37}$ coatings annealed for 1 h exhibited an XRD pattern comprising $TaAl_3$ and α-Ta phases, which was similar to those of the $Ta_{0.61}Al_{0.39}$ coatings annealed in 1% O_2–99% Ar at 600 °C for 4–24 h (Figure 6). The $Ta_{0.63}Al_{0.37}$ coatings annealed in air for 4 h demonstrated an amorphous and an orthorhombic Ta_2O_5 (ICDD 00–025–0922) phase. Moreover, the annealed $Ta_{0.63}Al_{0.37}$ coatings exhibited a Ta_2O_5 dominant structure after extending the annealing time to 12–100 h. The coating thickness increased from 792 to 924, 1098, 1220, 1565, 1687, and 1725 nm, while increasing the annealing time from 0 to 1, 4, 12, 24, 50, and 100 h by examining the cross-sectional SEM images (Figure 9). The 100 h annealed sample was well adhered on the substrate. Figure 10a,b displays the AES results of the $Ta_{0.63}Al_{0.37}$ coatings annealed in air at 600 °C for 1 and 12 h, respectively. The O diffused into a depth of 720 and 1220 nm (the entire annealed coating) for the 1 and 12 h annealed $Ta_{0.63}Al_{0.37}$ coatings, respectively. The variation of the O profile was consistent with the variation of the Al profile for the 1 h-annealed coatings, which indicated that the internal oxidation was conducted by the preferential formation of Al-oxide. However, the AES results of a 12 h annealed $Ta_{0.63}Al_{0.37}$ coating were classified into two parts. In the interior region, the variations of the O and Al profiles were consistent. By contrast, in the outer region, including six stacking layers, the positions with local maximum O levels were accompanied with high Ta contents, which implied that Ta-oxide formed after the inward diffusion of O, exceeding a demanded stoichiometric level for Al_2O_3.

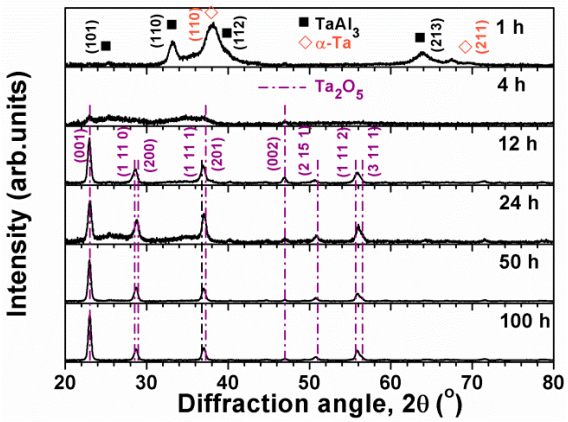

Figure 8. XRD patterns of $Ta_{0.63}Al_{0.37}$ coatings annealed in air at 600 °C.

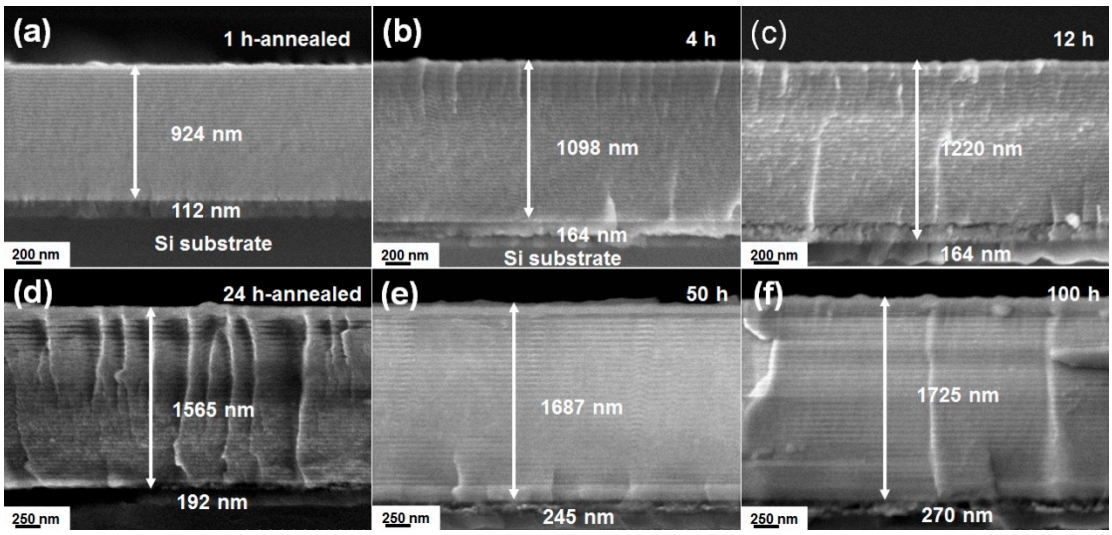

Figure 9. Cross-sectional SEM images of $Ta_{0.63}Al_{0.37}$ coatings annealed in air at 600 °C for (**a**) 1, (**b**) 4, (**c**) 12, (**d**) 24, (**e**) 50, and (**f**) 100 h.

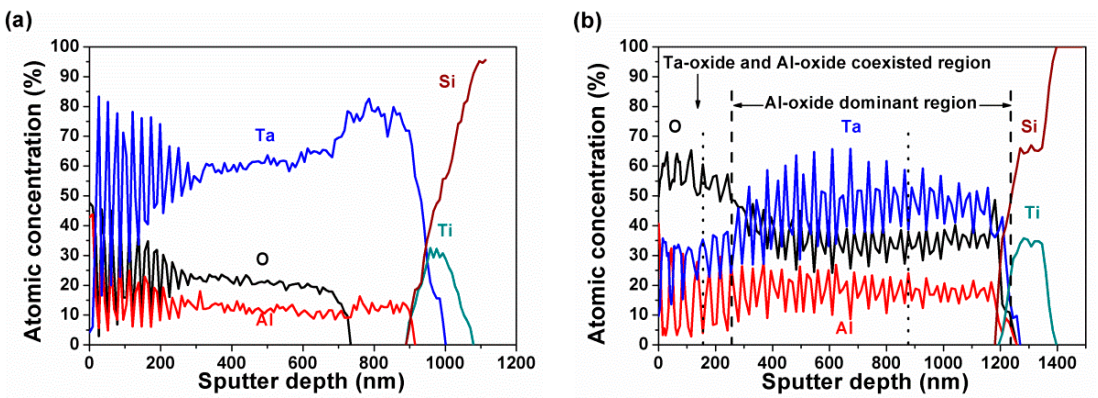

Figure 10. AES depth profiles of $Ta_{0.63}Al_{0.37}$ coatings annealed in air at 600 °C for (**a**) 1 and (**b**) 12 h.

Figure 11a shows the cross-sectional TEM image and SADPs of a $Ta_{0.63}Al_{0.37}$ coating after annealing in air at 600 °C for 12 h. The SADP of the outer region exhibited spots of an orthorhombic Ta_2O_5 phase which implied that the outer region comprised crystalline Ta_2O_5 and amorphous Al-oxide phases. By contrast, the SADP of the interior region exhibited a diffused ring of β-Ta phase. Figure 11b shows the EDS analysis results, which exhibit a decrease trend along the depth direction for the O content. The black sublayers exhibited high Ta and low Al compositions related to those of the white

sublayers. Figure 11c displays a high-resolution TEM image in the outer region, indicated in Figure 11a, which shows that the black sublayer is crystalline Ta_2O_5 and the white sublayers are amorphous. Figure 11d illustrates a high-resolution TEM image in the deeper interior region, the sublayers 23 and 24, which shows that the black sublayers comprise lattice fringes of $TaAl_3$ and β-Ta phases, and the white sublayers are amorphous.

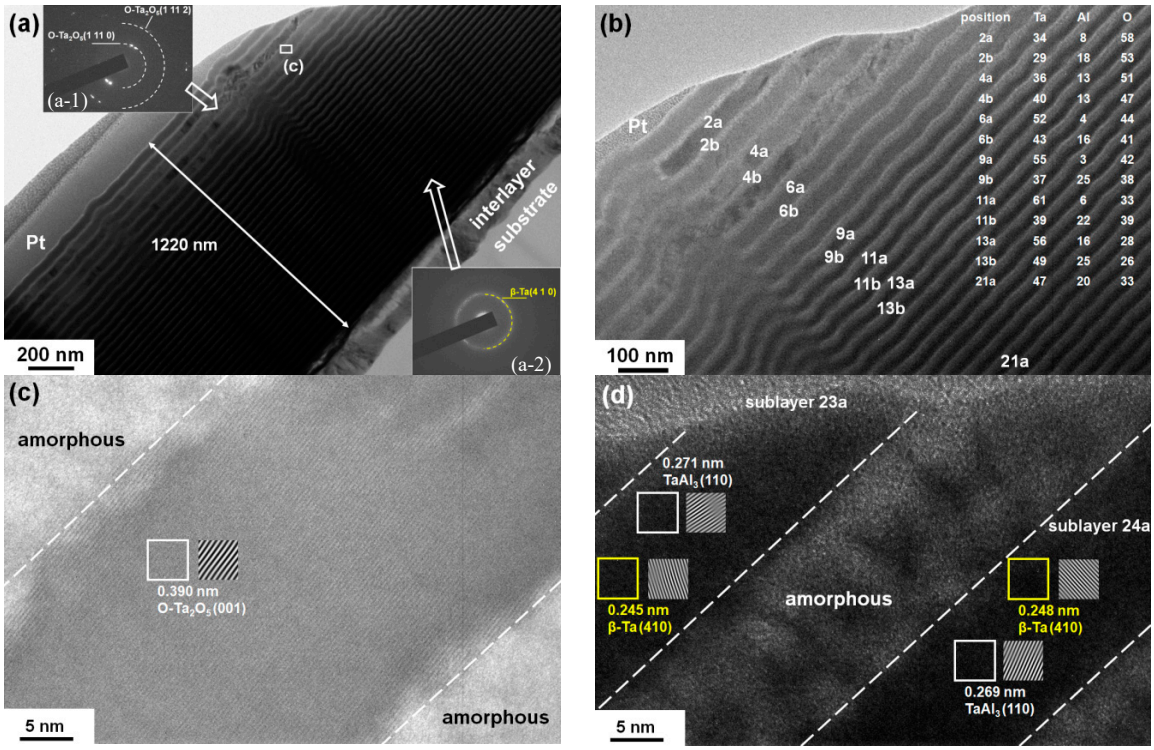

Figure 11. (**a**) Cross-sectional TEM image and (**a–1** and **a–2**) SADP, (**b**) EDS analysis results, (**c**) and (**d**) high-resolution TEM images of the $Ta_{0.63}Al_{0.37}$ coating annealed in air at 600 °C for 12 h.

4. Conclusions

The Ta–Al multilayer coatings were prepared by direct current magnetron co-sputtering through cyclical gradient concentration deposition which formed alternatively stacked Ta- and Al-rich sublayers. The preferentially formed oxides were amorphous Al_2O_3, and then orthorhombic Ta_2O_5 at 600 °C. The insolubility between Ta and Al resulted in the Ta-rich sublayers obstructing the diffusion of Al, whereas the Al-rich sublayers formed amorphous Al-oxide sublayers after annealing in O_2-containing atmospheres which restricted further oxidation; these effects caused the Ta-rich Ta–Al multilayer coatings to exhibit thermal stability and oxidation resistance when they were annealed up to 100 h at 600 °C in a 1% O_2–99% Ar atmosphere. Moreover, the multilayer structure of the $Ta_{0.63}Al_{0.37}$ coatings was maintained after annealing up to 100 h at 600 °C in air. The Ta–Al multilayer coatings exhibited the potential to replace the Ru–Al coatings utilized under oxygen containing atmospheres for high-temperature purposes such as bond coats in thermal barrier systems; therefore, the feature study should focus on the bond coat characteristics of the Ta–Al multilayer coatings, including the formation of a thermally grown oxide layer on the bond coats and the restricted oxidation behavior of multilayer coatings during the deposition of thermal barrier coatings.

Author Contributions: Conceptualization, Y.-I.C.; Funding acquisition, Y.-I.C.; Investigation, N.-Y.L. and Y.-E.K.; Project administration, Y.-I.C.; Validation, Y.-I.C. and Y.-E.K.; Writing—original draft, Y.-I.C.

Funding: This research was funded by the Ministry of Science and Technology, Taiwan, grant number 106-2221-E-019-022-MY3. The APC was funded by the National Taiwan Ocean University.

Acknowledgments: The authors thank Mei-Chen Chiang at Ming Chi University of Technology for technical support with TEM observations. The authors thank Su-Yueh Tsai at the Instrumentation Center at the National Tsing Hua University for technical support with the FE-EPMA analyses.

Conflicts of Interest: The authors declare no conflict of interest.

References

1. Mücklich, F.; Ilić, N. RuAl and its alloys. Part I. Structure, physical properties, microstructure and processing. *Intermetallics* **2005**, *13*, 5–21. [CrossRef]
2. Mücklich, F.; Ilić, N.; Woll, K. RuAl and its alloys, Part II: Mechanical properties, environmental resistance and applications. *Intermetallics* **2008**, *16*, 593–608. [CrossRef]
3. Mitsui, H.; Habazaki, H.; Hashimoto, K.; Mrowec, S. The sulfidation and oxidation behavior of sputter-deposited Al–Ta alloys at high temperatures. *Corros. Sci.* **1997**, *39*, 59–76. [CrossRef]
4. Habazaki, H.; Mitsui, H.; Ito, K.; Asami, K.; Hashimoto, K.; Mrowec, S. Roles of aluminium and chromium in sulfidation and oxidation of sputter-deposited Al- and Cr-refractory metal alloys. *Corros. Sci.* **2002**, *44*, 285–301. [CrossRef]
5. Gurrappa, I.; Wilson, A.; Datta, P.K. Palladium and tantalum aluminide coatings for high-temperature oxidation resistance of titanium alloy IMI 834. *J. Coat. Technol. Res.* **2009**, *6*, 257–268. [CrossRef]
6. Lee, J.W.; Kuo, Y.C. Cyclic oxidation behavior of a cobalt aluminide coating on Co-base superalloy AMS 5608. *Surf. Coat. Technol.* **2005**, *200*, 1225–1230. [CrossRef]
7. Das, D.K. Microstructure and high temperature oxidation behavior of Pt-modified aluminide bond coats on Ni-base superalloys. *Prog. Mater. Sci.* **2013**, *58*, 151–182. [CrossRef]
8. Wang, C.J.; Chen, S.M. The high-temperature oxidation behavior of hot-dipping Al–Si coating on low carbon steel. *Surf. Coat. Technol.* **2006**, *200*, 6601–6605. [CrossRef]
9. Bobzin, K.; Brögelmann, T.; Kalscheuer, C.; Liang, T. Al–Si and Al–Si–Y coatings deposited by HS-PVD for the oxidation protection of γ-TiAl. *Surf. Coat. Technol.* **2018**, *350*, 587–595. [CrossRef]
10. Zhu, L.; Du, G.; Bai, S.; Zhang, H.; Ye, Y.; Ai, Y. Oxidation behavior of a double-layer iridium-aluminum intermetallic coating on iridium at the temperature of 1400–2000 °C in the air atmosphere. *Corros. Sci.* **2017**, *123*, 328–338. [CrossRef]
11. Sen, S.; Lake, M.; Schaaf, P. Experimental investigation of high temperature oxidation during self-propagating reaction in Zr/Al reactive multilayer films. *Surf. Coat. Technol.* **2018**, *340*, 66–73. [CrossRef]
12. Wuu, D.S.; Chan, C.C.; Horng, R.H.; Lin, W.C.; Chiu, S.L.; Wu, Y.Y. Structural and electrical properties of Ta–Al thin films by magnetron sputtering. *Appl. Surf. Sci.* **1999**, *144–145*, 315–318. [CrossRef]
13. Su, P.J.; Chung, C.K. Amorphization of Ta–Al films using magnetron sputtering. *Surf. Coat. Technol.* **2005**, *200*, 1664–1668. [CrossRef]
14. Chung, C.K.; Chang, Y.L.; Chen, T.S.; Su, P.J. Annealing effects on microstructure and properties of Ta–Al thin film resistors. *Surf. Coat. Technol.* **2006**, *201*, 4195–4200. [CrossRef]
15. Hung, F.S. Material application of a transformer box: A study on the electromagnetic shielding characteristics of Al–Ta coating film with plasma-spray process. *Coatings* **2019**, *9*, 495. [CrossRef]
16. Chen, Y.I.; Zhang, Z.T.; Kai, W.; Huang, Y.R. Oxidation behavior of Ru–Al multilayer coatings. *Appl. Surf. Sci.* **2017**, *406*, 1–7. [CrossRef]
17. Chen, Y.I.; Tsai, B.N. Internal oxidation mechanism for Ta–Ru and Mo–Ru coatings. *Thin Solid Films* **2011**, *519*, 4974–4980. [CrossRef]
18. Chen, Y.I. Laminated structure in internally oxidized Ru–Ta coatings. *Thin Solid Films* **2012**, *524*, 205–210. [CrossRef]
19. Chen, Y.I.; Chu, H.N.; Chang, L.C.; Lee, J.W. Internal oxidation and mechanical properties of Ru based alloy coatings. *J. Vac. Sci. Technol. A* **2014**, *32*, 02B101. [CrossRef]
20. Chen, Y.I.; Huang, Y.R.; Chang, L.C. Internal oxidation of laminated Hf–Ru coatings. *J. Vac. Sci. Technol. A* **2016**, *34*, 02D103. [CrossRef]
21. Chen, Y.I.; Lu, T.S.; Zheng, Z.T. Internally oxidized Ru–Zr multilayer coatings. *Coatings* **2017**, *7*, 46. [CrossRef]
22. Kofstad, P. *High Temperature Corrosion*; Elservier Applied Science Publishing: New York, NY, USA, 1988.
23. Khanna, A.S. *Introduction to High Temperature Oxidation and Corrosion*; ASM International: Materials Park, OH, USA, 2002.

24. Chen, Y.I.; Zheng, Z.T.; Jhang, J.W. Thermal stability of Ru–Al multilayered thin films on Inconel 617. *Metals* **2018**, *8*, 514. [CrossRef]
25. Stavrev, M.; Fischer, D.; Wenzel, C.; Drescher, K.; Mattern, N. Crystallographic and morphological characterization of reactively sputtered Ta, Ta–N and Ta–N–O thin films. *Thin Solid Films* **1997**, *307*, 79–88. [CrossRef]
26. Shin, C.S.; Kim, Y.W.; Gall, D.; Greene, J.E.; Petrov, I. Phase composition and microstructure of polycrystalline and epitaxial TaN_x layers grown on oxidized Si(001) and MgO(001) by reactive magnetron sputter deposition. *Thin Solid Films* **2002**, *402*, 172–182. [CrossRef]
27. Chen, Y.I.; Chen, S.M. Annealing effects on nanostructure and mechanical properties of nanolaminated Ta–Zr coatings. *Surf. Coat. Technol.* **2013**, *215*, 209–217. [CrossRef]
28. Steidel, C.A. Electrical and structural properties of co-sputtered tantalum–aluminum films. *J. Vac. Sci. Technol.* **1969**, *6*, 694–698. [CrossRef]
29. Sina, H.; Iyengar, S.; Lidin, S. Reaction behavior and evolution of phases during the sintering of Ta–Al powder mixtures. *J. Alloy. Compd.* **2016**, *654*, 103–111. [CrossRef]
30. Barin, I. *Thermochemical Data of Pure Substances*, 3rd ed.; VCH: New York, NY, USA, 1995.
31. Seifert, M.; Rane, G.K.; Oswald, S.; Menzel, S.B.; Gemming, T. The influence of the composition of $Ru_{100-x}Al_x$ (x = 50, 55, 60, 67) thin films on their thermal stability. *Materials* **2017**, *10*, 277. [CrossRef]
32. Chen, Y.I.; Jhang, J.W. Thermal stability of laminated Ru–Al/Ru–Al–Zr coatings on Inconel 617. *Surf. Coat. Technol.* **2019**, *361*, 357–363. [CrossRef]
33. Kattner, U.R. Ta-Al Phase Diagram. In *Binary Alloy Phase Diagrams*; Massalski, T.B., Ed.; ASM International: Materials Park, OH, USA, 1990.
34. Witusiewicz, V.T.; Bondar, A.A.; Hecht, U.; Zollinger, J.; Petyukh, V.M.; Fomichov, O.S.; Voblikov, V.M.; Rex, S. Experimental study and thermodynamic re-assessment of the binary Al–Ta system. *Intermetallics* **2010**, *18*, 92–106. [CrossRef]